UNIVERSITY
OF WOLLONGONG
AUSTRALIA

University of Wollongong
Research Online

Faculty of Science, Medicine and Health - Papers

Faculty of Science, Medicine and Health

2015

Strand separation establishes a sustained lock at the Tus-Ter replication fork barrier

Bojk A. Berghuis
Delft University of Technology

David Dulin
Delft University of Technology

Zhi-Qiang Xu
University of Wollongong, zhiqiang@uow.edu.au

Theo van Laar
Delft University of Technology

Bronwen Cross
Delft University of Technology

See next page for additional authors

Publication Details

Berghuis, B. A., Dulin, D., Xu, Z., van Laar, T., Cross, B., Janissen, R., Jergic, S., Dixon, N. E., Depken, M. & Dekker, N. H. (2015). Strand separation establishes a sustained lock at the Tus-Ter replication fork barrier. Nature Chemical Biology, 11 (8), 579-585.

Research Online is the open access institutional repository for the University of Wollongong. For further information contact the UOW Library: research-pubs@uow.edu.au

Strand separation establishes a sustained lock at the Tus-Ter replication fork barrier

Abstract

The bidirectional replication of a circular chromosome by many bacteria necessitates proper termination to avoid the head-on collision of the opposing replisomes. In Escherichia coli, replisome progression beyond the termination site is prevented by Tus proteins bound to asymmetric Ter sites. Structural evidence indicates that strand separation on the blocking (nonpermissive) side of Tus-Ter triggers roadblock formation, but biochemical evidence also suggests roles for protein-protein interactions. Here DNA unzipping experiments demonstrate that nonpermissively oriented Tus-Ter forms a tight lock in the absence of replicative proteins, whereas permissively oriented Tus-Ter allows nearly unhindered strand separation. Quantifying the lock strength reveals the existence of several intermediate lock states that are impacted by mutations in the lock domain but not by mutations in the DNA-binding domain. Lock formation is highly specific and exceeds reported in vivo efficiencies. We postulate that protein-protein interactions may actually hinder, rather than promote, proper lock formation.

Disciplines

Medicine and Health Sciences | Social and Behavioral Sciences

Publication Details

Berghuis, B. A., Dulin, D., Xu, Z., van Laar, T., Cross, B., Janissen, R., Jergic, S., Dixon, N. E., Depken, M. & Dekker, N. H. (2015). Strand separation establishes a sustained lock at the Tus-Ter replication fork barrier. Nature Chemical Biology, 11 (8), 579-585.

Authors

Bojk A. Berghuis, David Dulin, Zhi-Qiang Xu, Theo van Laar, Bronwen Cross, Richard Janissen, Slobodan Jergic, Nicholas E. Dixon, Martin Depken, and Nynke H. Dekker

This journal article is available at Research Online: http://ro.uow.edu.au/smhpapers/2991

Strand separation establishes a sustained lock at the Tus–*Ter* replication fork barrier

Bojk A. Berghuis[1], David Dulin[1], Zhi-Qiang Xu[2], Theo van Laar[1], Bronwen Cross[1], Richard Janissen[1], Slobodan Jergic[2], Nicholas E. Dixon[2], Martin Depken[1] & Nynke H. Dekker[1*]

[1]Department of Bionanoscience, Kavli institute of Nanoscience, Delft University of Technology, Lorentzweg 1, 2628 CJ Delft, The Netherlands

[2]Centre for Medical and Molecular Bioscience and School of Chemistry, University of Wollongong, New South Wales 2522, Australia

* Correspondence may be addressed to n.h.dekker@tudelft.nl.

ABSTRACT

The bidirectional replication of a circular chromosome by many bacteria necessitates proper termination to avoid the head-on collision of the opposing replisomes. In *E. coli*, replisome progression beyond the termination site is prevented by Tus proteins bound to asymmetric *Ter* sites. Structural evidence indicates that strand separation on the blocking (non-permissive) side of Tus–*Ter* triggers roadblock formation, but biochemical evidence also suggests roles for protein–protein interactions. Here, DNA unzipping experiments demonstrate that non-permissively oriented Tus–*Ter* forms a tight lock in the absence of replicative proteins, while permissively oriented Tus–*Ter* allows nearly unhindered strand separation. Quantifying the lock strength reveals the existence of several intermediate lock states that are impacted by mutations in the lock domain, but not by mutations in the DNA-binding domain. Lock formation is highly specific and exceeds reported in vivo efficiencies. We postulate that protein–protein interactions may actually *hinder* rather than promote proper lock formation.

INTRODUCTION

DNA replication in *Escherichia coli* initiates bidirectionally at *oriC,* creating two replication forks that proceed around the circular 4.6 Mbp chromosome in opposite directions. The forks progress at an average speed of 1 kbp/s until they meet again at the terminus region. As the replication forks approach the terminus, each encounters five 23 bp *Ter* DNA sites bound in a specific orientation by a 36 kDa DNA binding protein called Tus[1–4], and proceeds unhindered. However, when a replication fork continues beyond the terminus, Tus–*Ter* is approached from the opposite direction (**Fig. 1a**), triggering Tus–*Ter* to form a tightly locked complex, thereby bringing the replication fork to a halt[1,5–7]. Each *Ter* site is non-palindromic, does not contain any direct repeats and has a strictly conserved GC6 base pair followed by a highly conserved 13 base-pair core region. Tus is a monomeric protein that forms a simple 1:1 complex with *Ter*[8] (**Fig. 1b**). The structure of the Tus–*TerA* complex shows that many of the conserved residues among the *Ter* sites make base-specific contacts with the protein[4,9]. The Tus–*TerB* complex has a reported dissociation constant (K_D) of 44 pM in 50

mM NaCl[10]. This renders it the most stable complex known between a monomeric sequence-specific DNA-binding protein and a duplex DNA recognition sequence.

A long-standing issue regards the manner in which the asymmetric blockage at Tus–*Ter* comes about. Does Tus itself function as a molecular roadblock, locking itself onto the *Ter* DNA as the DNA replication machinery approaches, or are there specific protein–protein interactions that lead to the polar arrest of the replisome? On one hand, various studies imply specific protein–protein interactions between Tus and the replicative helicase, DnaB. Tus–*Ter* is much more effective in its natural host for instance, while the functionally similar but structurally unrelated *Bacillus subtilis* replication termination system works well in *E. coli*[11,12]. Tus–*Ter* blocks DnaB *in vitro,* but not the Rep helicase[13], and evidence from yeast two-hybrid analysis shows specific interactions between DnaB and Tus[14]. On the other hand, ample evidence suggests a protein-independent polar blocking mechanism. For example, RNA chain elongation catalyzed by T7, SP6 and *E. coli* RNA polymerases is impeded by Tus–*Ter* in a polar manner[15,16]. Tus–*TerB* also blocks the actions of UvrD, Rep, PriA, and SV40 large T antigen helicases, indicating low specificity for DnaB alone[17–20].

In 2006 light was shed on this molecular roadblock through surface plasmon resonance (SPR) studies of dissociation of Tus from forked *TerB* oligonucleotides, supported by a crystal structure of a forked, "locked" Tus–*Ter* complex. This locked complex exhibits significant structural changes at the fork-blocking (non-permissive) face in comparison with the ds*TerA*-bound, but not locked, structure elucidated a decade earlier[4,21]. The locked conformation reveals that of the ssDNA bases in the forked *Ter* region (*Ter* bases 1–7), the highly conserved C6 base is flipped out of the helical DNA axis and into the protein (**Fig. 1c**). In this conformation the C6 base undergoes tight interactions with several amino acids (**Fig. 1d**). These Tus lock domain residues are distinctly different from those involved in sequence recognition and binding affinity[22]. It was therefore proposed that the Tus–*Ter* system is the molecular analog of a mousetrap: the trap is set by Tus binding to *Ter* in an oriented fashion, and triggered by strand separation invoked by the approaching replication machinery[21].

The mousetrap model has two major implications. First, it suggests that binding and lock formation are two different mechanisms that can be ascribed to different domains of Tus. Secondly, lock formation through strand separation could occur independently of any specific protein–protein interactions. Nevertheless, convincing evidence arose that translocation of DnaB on dsDNA in the absence of unwinding is sufficient to provoke polar arrest[23]. Although this result does not require it, these authors propose an alternative model in which the DnaB helicase binds specifically to Tus, arguing that the locked complex formation might act as a backup mechanism when protein–protein interaction fails, but may not be sufficient on its own.

In this study, we used the quantitative power of high-throughput single-molecule approaches to address both of the key implications of the Tus–*Ter* mousetrap model and to dissect the overall mechanism of lock formation. By applying mechanical force to unwind a DNA hairpin containing a single *TerB* site, we mimic replisome-mediated DNA unwinding and directly show that strand separation alone can trigger the non-permissively oriented Tus–*Ter* to form a strong and long-lived lock. Remarkably, the Tus–*Ter* lock formed in 100% of our hairpin opening attempts. This is in contrast to Tus–*Ter* in the permissive orientation: here strand separation proceeded virtually unhindered. We are able to quantify the lock strength by measuring the lifetimes of the Tus–*Ter* complex at different forces. These experiments reveal that at high forces, Tus dissociation occurred on three (or more) characteristic timescales, suggesting that strand separation at high forces partitions the Tus–*Ter* structure into thermodynamically trapped sub-structures. We argue that the shorter-lived sub-structures correspond to intermediates in the process of full lock formation during replisomal strand separation, and that the longest-lived structure is the full lock.

Our results strongly validate the molecular mousetrap model[21] by showing that Tus–*Ter* causes polar arrest of strand separation in the absence of any replication-related proteins. We show that the interaction formed is efficient and not limited by the rate of C6 flipping and finding the lock pocket. Using specific mutants, we were able to discriminate DNA binding and locking domains in this system. Residue H144, located deep in the Tus lock domain, determines the strength of interaction of the Tus–*Ter* lock: force-dependent lifetimes of H144A decreased more profoundly than those of any of the other single-site mutations tested. F140, located at the side of the lock pocket, was found to be involved in the specificity of the lock pocket for a C-base. Interestingly, residue E49, located outside the lock domain and thought to play a pivotal role in the specific interaction of Tus with DnaB, displayed a marked decrease in the probability of lock formation while the lock lifetime was identical to wild-type (wt) Tus–*Ter*. This shows that E49 plays a crucial role in guiding C6 to the lock domain, and that interfering with specific residues surrounding the Tus lock modulates the probability of forming a tightly locked Tus–*Ter* complex. Conversely, a mutation in the DNA-binding domain at the permissive face of the complex does not affect the locking behavior. As *in vivo* experiments thus far point towards molecular motor arrest probabilities significantly below[12] those found here, we hypothesize that protein–protein interactions, rather than forming the basis of promoting polar arrest, might actually perform the opposite function of *hindering* proper lock formation. Our assay resolves the controversy that still surrounds this protein–DNA complex by providing direct insight into how different DNA processing enzymes in a head-on collision with Tus–*Ter* can exhibit varying blocking efficiencies, in particular by modulating the probability of lock formation through (non-specific) steric hindrance.

RESULTS

Mimicking DNA replication fork progression using DNA hairpins

We set up a single-molecule assay using magnetic tweezers and DNA hairpins, allowing us to controllably invoke the double-stranded DNA unwinding that normally accompanies DNA replication, only now in the absence of the replication proteins. Our experiments initially comprised three DNA hairpin designs with specific sequences inserted at their midpoints: the first hairpin contains a single *TerB* site in the permissive orientation (**Fig. 2a**); the second has the *TerB* site inverted, forming the non-permissive orientation (**Fig. 2b**); and lastly, the third hairpin contains a *TerB* site in the non-permissive orientation, but now including a point mutation at the GC6 site in which the highly conserved C6 base has been replaced by a guanine (GC-flip) (**Supplementary Results, Supplementary Fig. 1b**). As the mousetrap model suggests a purely mechanical interaction of Tus–*Ter* upon strand separation, it predicts that in our setup lock formation should still occur in one direction (non-permissive) but not the other (permissive). If protein–protein interactions were essential for proper lock formation, lock formation should at most be infrequent in our assay. We detected lock formation through the difference in extension between a hairpin that is fully opened and one that is blocked halfway.

Tus–*Ter* blocks force-induced unwinding

At low forces (<16 pN), base-paired DNA is energetically more favorable than single-stranded DNA, so the hairpin remains closed[24–26]. Upon increasing the force (>16 pN) in the absence of Tus, the hairpin opens, which can be seen as a rapid increase in extension for both the permissive and the non-permissive hairpin (**Fig. 2c,d**, red traces). Repeating this experiment in the presence of Tus, the outcome was almost identical for the permissive *Ter* hairpin (**Fig. 2c**, blue trace): here Tus–*Ter* interaction left only a transient signal upon hairpin opening (**Supplementary Fig. 2h**). In contrast, the results were very different for the non-permissive hairpin (**Fig. 2d**, blue trace): here the maximal extension in the presence of Tus was only half of the fully opened hairpin, indicating that strand separation is blocked exactly at the *Ter* site (see Online Methods and **Supplementary Fig. 1a**). This behavior was observed for non-permissive hairpins in 100% of the experiments at 50 mM KCl and a Tus concentration of 2 nM. Increasing the ionic strength to 350 mM resulted in a modest decrease in the occurrence of blocking, but did not affect the lock strength (**Supplementary Fig. 2d–f**). The high efficiency of lock formation still occurred despite the fact that in our experiments the DNA helix is unwound at a rate of ~30 kbp·s^{-1} (**Supplementary Fig. 1c**), at least 10-fold faster than any replisome would unwind DNA. Increasing the force shows that the Tus–*Ter* lock remains in place at forces up to 60 pN, showing the remarkable strength of this locked complex. This experiment thus validates the proposed protein–protein independency[21] and strongly suggests that this mechanism alone is readily equipped for the task of blocking an approaching replication fork, other helicases and transcription machinery alike.

Lock breakage shows different degrees of lock formation

We measured the distribution of constant-force lock dwell times for all protein and *Ter* variants (**Fig. 2e**), taking advantage of the natural force clamp mode and multiplexing capacity of magnetic tweezers. The distributions are highly reproducible and contain force-specific as well as mutant-specific signatures (**Fig. 3b,c**; **Supplementary Fig. 2a–c**). A main feature of all lock dwell time distributions is that they are (multi)exponentially distributed, reflecting the stochastic nature of lock rupture (**Fig. 2f**). We found that the distributions contain, according to the Bayes-Schwartz information criterion[27], two or three exponentially distributed states, depending on the type of Tus–*Ter* interaction investigated. We used maximum likelihood estimation to fit the data (**Fig. 2f**)[28], and obtained confidence intervals through bootstrapping[29] as described previously[30]. As these high-force measurements place a large tension on the DNA tethers, choosing the right force is a trade-off between tether lifetime[31] and the ability to resolve the different lock states (**Supplementary Fig. 1d**). Typically, we chose the force such that 3-exponential datasets exhibited a first short-lived exponential with a lifetime of ~1 s, a second exponential with a lifetime on the order of 10 s and a third, long-lived exponential on the order of 100 s.

In examining Tus locking behavior, it is convenient to consider this system through a lock-and-key analogy, where the C6 base is the key that fits into the Tus lock pocket (**Fig. 3a**). In this analogy, the interaction between wt Tus and non-permissive *Ter* should provide a signature analogous to a perfect match between key and keyhole (**Fig. 3a**, wt Tus–*Ter*). We found the force-dependent dwell times of the wt Tus–*Ter* lock to be distributed over three states, with the longest-lived exponential distribution having a lifetime of ~720 s at 59 pN (**Fig. 3b,c**, purple circles). The shortest-lived exponential state at 59 pN had a lifetime of ~1 s, and the intermediate state a lifetime of ~30 s. The lifetimes of all three states decreased in a concerted fashion as the force was increased, with the longest-lived distribution having a lifetime of 54 s at 93 pN (**Fig. 3c, Supplementary Table 1**). We also observed a force-dependent probability of forming the longest-lived state: while at 93 pN there was a mere 7% chance for a dwell time to belong to the longest-lived state, this probability increased to 73% at 59 pN (**Fig. 3d**). Conversely, trapping the system in one of the shorter-lived states became progressively less likely as the force was decreased (**Supplementary Fig. 2i**). The force-dependent probability of all states also indicated that the first two states likely represent intermediate conformations that occur at all forces, while the longest-lived state is the full lock. Thus when the magnetic tweezers exert their highest forces, they prevent the short-lived conformations from proceeding to the fully locked state, while the longest-lived state predominates at low forces.

Experiments on permissive wt Tus–*Ter* resulted in sharply reduced dwell times that obeyed a single-exponential distribution with a mean of 0.8 s at 19 pN (**Fig. 3c**, purple square; **Supplementary Fig. 2h**); at

higher forces, dwell times were too short to be detected. In fact, there is no single force at which both non-permissive and permissive dwell times can be measured: the dwell times of non-permissive wt Tus–*Ter* become too long at 19 pN for practical measurements (see **Supplementary Fig. 1d**). This implies that none of the states we found for the non-permissive orientation can be attributed solely to the binding of Tus. To further investigate the origin of the observed states, we can compare the changes in lifetime and probability invoked by mutations in Tus and/or *TerB*.

Mutations in binding domain need not hamper lock formation

The crystal structure of the locked wt Tus–*Ter* shows that DNA sequence recognition and binding can be largely attributed to a DNA binding domain that primarily consists of 2 antiparallel β-strands that interact with the major groove of *Ter* DNA (**Fig. 1b**). Site-specific mutation in the DNA binding domain (Q250A, **Supplementary Fig 3e**) is known to result in a sharp increase of the K_D[22], but whether it affects lock kinetics is unknown. In our experiments, Q250A exhibited dwell time distributions very similar to those of wt Tus at the same forces (**Fig. 3c**, cyan). We saw no correlation between the K_D of Tus–ds*TerB* and lock strength. From this we conclude that lock formation is not severely affected by a change in the binding domain.

The C6 base is crucial and not rate-limiting for lock formation

We subsequently set out to examine the effect that changing the key, i.e. the C6 base (**Fig. 3a,** switch from green to magenta key), had on the wt Tus–*Ter* lifetimes. A single base pair inversion of the *TerB* sequence at position 6 profoundly affects the fork arrest efficiency[32]. In our experiments, inversion of GC6 indeed had a dramatic effect on the lifetimes (**Fig. 3c**, purple triangles), as the dominant lifetime was no greater than 1 s at 40 pN. By comparison, the dominant lifetime of wt Tus–*Ter* is at least two orders of magnitude higher based on extrapolation of the lifetimes of the fully locked state observed in the range 59–93 pN (**Fig. 3c**, purple circles). Despite the decrease in observed lifetimes, the G6 *Ter* site continued to impose an increased barrier to hairpin opening, as the lifetimes remain well above those found for binding only (**Fig. 3c**, purple square). For wt Tus with the modified key, we found the presence of two states (**Supplementary Fig. 2g**, purple), with the longest-lived lifetime decreasing from 39 to 0.7 s in the 29–40 pN range (**Fig. 3c**, purple triangles and dashed line). We also assessed whether uncoupling lock formation from mechanical probing (by creating a hairpin containing an unpaired region of 5 bases containing C6, see **Supplementary Fig. 1b**) would populate the fully locked state even at high forces, as it is known that this 5-base mismatch dramatically increases the affinity of the Tus–*Ter* complex[21]. The resulting state-probabilities however, were identical to that of normal wt Tus–*Ter* (**Fig. 4a**), indicating pre-formation of the lock does not alter the state populations.

Probing mechanism via mutations in or near the lock domain

To investigate how the *Ter* key enters the Tus lock, we performed experiments on a series of Tus mutants altered in or near the lock domain. Two amino acid residues H144 and F140 are situated directly in the lock domain, and based on the crystal structure their roles differ in a subtle, though significant manner. Residue H144 lies deep within the lock pocket and interacts only with the C6 base. Mutation to H144A removes the imidazole ring as well as a positive charge, leaving a cavity deep within the pocket (**Supplementary Fig. 3b**, in blue). In our lock-and-key representation, we depict this by changing the inner shape of the lock (**Fig. 3a**, light blue). Amino acid residue F140 lies closer to the outer edge of the lock pocket than H144. F140 still interacts with C6, and a stacking interaction of the phenyl ring with the adjacent A7 base is also present (**Supplementary Fig. 3c,** in orange). Removal of the phenyl ring in the F140A mutant will thus lead to a gap at the edge of the lock pocket, which can be depicted as a widening of the keyhole (**Fig. 3a**, orange). Residue E49, linked to the putative specific protein–protein interaction between Tus and the *E. coli* DnaB helicase[13,14], lies just outside the lock domain (**Supplementary Fig. 3d**, in green), though it does make a water-mediated hydrogen-bonding contact with the 5'-phosphate of A7 in the locked complex[21]. The shape of the lock pocket remains unaffected by this mutation (**Fig. 3a**, green keyhole identical to wt).

Lock mutant F140A affects specificity, H144A affects strength.

We found that mutant F140A showed a marked decrease in dwell times at 59 pN (**Fig. 3b**, orange). Fitting revealed that the longest-lived exponential now has a lifetime of ~55 s, compared to 720 s for wt Tus at the same force (**Fig. 3c**, orange circles and solid line). We also observed that this third, longest-lived state has all but disappeared: the probability of entering this state is reduced from 73% for wt Tus to 1.8% for F140A in the same regime (**Fig. 3b**,orange: note the absence of counts >100 s; **Fig. 3e**, orange bar in 'full lock' column). Thus, F140 appears to give rise to the third, long-lived state observed in Tus species with an intact lock pocket, and as such plays a role in the probability of forming a fully locked state. Similar to wt Tus, the probability exhibited a clear force-dependence: decreasing the force to 47 pN increased full lock probability to 31% (**Fig. 3d**, orange). Combining F140A with the mutated *Ter* site (**Fig. 3a**, magenta key with orange lock) further reduced the force-dependent lifetimes, but the resulting force-dependent lifetimes exceeded those of wt Tus with the mutated *Ter* site (**Fig. 3c**, orange triangles and dashed line; **Supplementary Fig. 2g**, orange). This apparent increase in lock strength in the presence of an altered key indicates that mutation of F140 leads to a decreased specificity for allowing only the C6 base into the lock.

Replacing H144 led to a more substantial decrease in Tus–*Ter* lock dwell times than F140A (**Fig. 3b,c**, blue circles). The dominant lifetime extracted at 59 pN was found to be ~2 s, whereas those of wt Tus and Q250A at the same force lie two orders of magnitude higher. The datasets were found to exhibit lifetimes measurable over a wide range of forces (24–59 pN), and all retained three exponential states. At 59 pN,

H144A led to a larger drop in the probability of entering the third, longest-lived state than mutation F140A: from 73% for wt Tus, this became 0.7% (**Fig. 3e**, blue). As observed for F140A and wt Tus, there is also a clear force-dependence of the probability to form a fully locked state for H144A: the probability increased to 26% at 24 pN (**Fig. 3d**, blue line). While mutation H144A is the single-site mutation with the largest effect on lock lifetimes, the decrease was not as severe as wt Tus with the G6 *Ter* site. When combining the H144A lock mutant with the mutated *Ter* site (**Fig. 3a**, magenta key with blue lock), the resulting distribution (0.5 s at 19 pN, **Fig. 3c**, blue circle) was not unlike that obtained for permissively oriented wt Tus (0.8 s at 19 pN, **Supplementary Fig. 2h**, blue). This indicates that H144A wt *Ter* lifetimes result from the specific interactions of the C6 base with the remaining amino acid residues in the lock pocket; further modification of the key within this altered lock results in the loss of all locking interactions.

E49K decreases the probability of lock formation.

For E49K we obtained a distribution of dwell times at 59 pN that contained the same three exponentially distributed states as wt Tus–*Ter* (**Fig. 3b**, green), with a longest-lived state lifetime of 933 s (720 s for wt). However, the probability of this state decreased significantly from 73% for wt to 6% for E49K (**Fig. 3e**). The first two exponentials fully overlapped with the two shortest-lived for F140A (**Fig. 3b**, orange). This suggests that the DNA-phosphate interaction with E49 is crucial for guiding the C6 base into its pocket to form the fully locked state. Mutating the *TerB* site (**Fig. 3a**, magenta key with green lock) caused a loss of almost all dwell times above ~1 s for forces above 26 pN, similar to the barrier imposed by Tus–*Ter* in the permissive orientation (**Supplementary Fig. 2g**). However, closer inspection revealed longer-lived events with a low probability of ~1.5% (**Supplementary Fig. 2h, Supplementary Table 2**); when extrapolated to higher forces, the longer-lived lifetimes (**Fig. 3c**, green triangles) resembled the much more probable states found for wt Tus interacting with the mutated *Ter* site in the 29–40 pN range (**Fig. 3c**, purple triangles, **Supplementary Table 2**). This indicates that while the wt lock domain continues to interact with the incorrect G6 key, mutation of E49 renders such an interaction very unlikely. Our observations clearly link the change invoked by E49K to a change in probability of forming the third, fully locked state.

Given all observations, we propose a kinetic model for wt lock formation containing three states (**Fig. 4b**). In this model, the Tus–*Ter* complex strengthens progressively and irreversibly as passage from one stable state to the next proceeds until the final, fully locked and longest-lived state is reached. Fitting revealed that loss of the long-lived lock state as force is increased is not due to slower transitions to stronger lock states (**Fig. 4c**, k_{12} and k_{23}), but rather to increased rate of disruption (k_{10}, k_{20} and k_{30}) of the lock states, as the force-dependent trends in these rates showed.

DISCUSSION

Our results have important implications for understanding of how the Tus–*Ter* lock is formed. We can directly discard the notion that Tus–*Ter* requires specific interaction with DnaB to form a stable lock and block replication fork progression for extended times. Our results strongly suggest that strand separation followed by specific interaction of the *Ter* C6 base with the Tus lock domain is the only mechanism needed for polar arrest. Evidence for this can be found in the fact that lock probabilities and lifetimes are affected by mutations in the lock domain, or mutation of the C6 base, but not by a mutation in the DNA binding domain. We further observed that mutant E49K, which is hypothesized to be deficient in polar replication fork arrest due to the elimination of specific protein–protein interactions[13,14], gave rise to lifetimes identical to that of wt Tus, only now with a severely decreased probability of entering the longest-lived state. This ties the observed deficiency of *in vivo* fork arrest to the drop in occurrence of the longest-lived state found in our experiments. In other words, the longest-lived state is likely to be the native lock conformation implicated in *in vivo* fork arrest, and residue E49 is shown to be part of the mechanism that facilitates formation of a tight interaction between C6 and the lock pocket.

Our experiments also demonstrate that flipping of the C6 base and subsequent interactions with the Tus lock pocket is not a rate-limiting step in the lock formation process. This is supported by our observation that there is little force-dependence in the inter-state rates (k_{12} and k_{23}, **Figure 4b,c**); in other words, the force-dependence of state probabilities is caused solely by the force-dependent state exit rates (k_{10}, k_{20} and k_{30}). As force influences the speed of strand separation and thus the time available for C6 flipping, while not affecting the inter-state transfer rates, the C6 flipping is likely not rate-limiting at the comparatively low unwinding velocities (**Supplementary Fig. 1c**) of the *E. coli* replisome.

This notion is strengthened further by our observation that pre-formation of the lock yielded a distribution of dwell times identical to normal Tus–*Ter* (**Fig. 4a**). In the pre-formed lock situation, it can be assumed that the C6 base has reached its equilibrium lock position. Our results imply that our pulling experiment provides sufficient time for this equilibration, even though the pulling experiment as a whole is a system in non-equilibrium. This is directly understood by comparing the typical timescales of DNA unwinding and the timescale of molecular rearrangement of the DNA bases upon disruption of Watson-Crick base pairing (**Fig. 4d**). The unwinding rate of DNA by a replisome is of the order of 1 kbp/s, and in our pulling experiments this rate is ~30 kb/s. Typical molecular single-bond rotations are known to take place on femtosecond to picosecond timescales, with larger scale motions like lock formation likely occurring in the nanosecond to microsecond range[33–35]. This implies that there is at least several orders of magnitude difference between the

rate of unwinding and the rate at which flipping of C6 and concomitant molecular rearrangements take place, leaving ample time for C6 to reach its equilibrium locked conformation.

The interpretation that the longest-lived state is the native or full lock state implies that the probability of native lock formation is significantly lower than 100% at the highest forces measured (**Fig. 3d**, purple). The force-dependent lock probabilities do however suggest that the full lock is the dominant state at low forces for wt Tus, and suggest that the mutant with the lowest full lock probability (H144A) may still have a significant chance of blocking an approaching replisome. A more direct link between our probabilities and *in vivo* arrest efficiencies will require knowledge of, for example, the amount of work performed by a replisome. It remains to be determined to what extent the two shortest-lived lock states are capable of causing arrest of DNA-processing enzymes, though the reported replisome arrest deficiency of E49K[13,14] together with our observation that E49K affects only the longest-lived state, suggests that these intermediate states are not sufficient to block replication fork progression. It is clear though that these two 'lesser' lock states still pose a significant barrier to strand separation, much more so than the mere binding of Tus alone.

The difference between the high efficiency of reaching the full-lock state in our experiments and the lower efficiencies of replisome arrest observed *in vivo*[12] must have a cause arising from interactions not captured in our experiments. These interactions might be invoked by the presence of an enzyme running into Tus–*Ter*. Steric effects, i.e., functional protein–protein interactions, could then be the cause of the observed decrease in efficiency. Thus, instead of providing the basis of fork arrest, functional interactions could have an antagonistic effect *in vivo*. Our experiments with mutant E49K suggest a possible mechanism: as the mutation in the Tus protein modulates the probability of forming the fully locked state without affecting the lifetime of the lock, an enzyme running into Tus–*Ter* could invoke a similar effect through functionally interacting with that same residue. Our experiments with wt Tus and E49K then respectively set the upper (no interaction, thus high lock probability) and lower (E49 function completely disrupted, low lock probability) boundaries of blocking probabilities. Two different enzymes that run into non-permissive Tus–*Ter* can then in turn have their own characteristic probabilities of being blocked due to the different ways these enzymes non-specifically interact with Tus residues such as E49 upon collision.

ACKNOWLEDGMENTS

We thank Jelmer Cnossen for his countless efforts in adjusting the MT software to our needs, Jacob Kerssemakers for discussions, and Samir Hamdan for his contribution to the discussion by generously sharing his own experimental observations. This study was supported by a grant of the Australian Research Council (DP0877658) to N.E.D. and a Vici grant from the Netherlands Organisation for Scientific Research to N.H.D.

AUTHOR CONTRIBUTIONS

N.E.D and N.H.D. designed the research. B.A.B. and N.H.D. designed the experiments. D.D. designed and assembled the magnetic tweezers apparatus. B.A.B. performed the experiments. B.A.B., B.C., T.L., R.J. and N.H.D. designed, and B.C. and T.L. made the DNA hairpin constructs. Z-Q.X. and S.J. purified the Tus proteins. B.A.B. and M.D. analyzed the data. M.D. developed the application of MLE to force spectroscopy data. B.A.B., D.D., M.D. and N.H.D. interpreted the data. S.J. and N.E.D. contributed to discussions concerning the model and *in vivo* observations. B.A.B., N.E.D. and N.H.D. wrote the paper.

COMPETING FINANCIAL INTERESTS

The authors declare no competing financial interests.

FIGURE CAPTIONS

Figure 1 The Tus–*Ter* complex structure and domains. (**a**) Location and orientation (turquoise for permissive, red for non-permissive face) of 23 base pair *Ter* sites in the *E. coli* chromosome. (**b**) The crystal structure of the locked Tus–*Ter* complex (PDB ID: 2I06) with a schematic representation directly below showing the protein has a DNA binding domain located mainly in the two antiparallel β-strands interacting with the major groove of *Ter* DNA (dark blue for base-specific interactions, light blue for non-specific interactions), as well as a lock domain (orange) where several amino acid residues interact specifically with C6 upon strand separation (**c**, **d** orange).

Figure 2 Magnetic tweezers assay used to quantify Tus–*Ter* lock mechanism. Schematic overview of a permissive (**a**, **c**) and a non-permissive (**b**, **d**) Tus–*Ter* experiment. (**a**) In the permissive experiment, force-induced DNA strand separation causes weakening of the interaction between Tus DNA-binding domain and the *Ter* site, with subsequent disruption of the Tus–*Ter* interaction. (**c**) In our MT DNA hairpin experiment, this implies full opening of the hairpin, yielding almost identical force extension curves for hairpins with or without Tus (blue and red respectively, dotted lines represent reannealing of the hairpin during force decrease). (**b**) With the non-permissively oriented *Ter* on a DNA hairpin, strand separation will first cause the C6 base to flip into the high-affinity protein-binding pocket of Tus, resulting in a locked Tus–*Ter* complex. In

other words, strand separation in our non-permissive hairpin will be blocked in the presence of Tus, resulting in an extension that is halved (**d**, blue) compared to the same hairpin in the absence of Tus (**d**, red). (**e**) To quantify lock behavior, we measure lock dwell times under constant force. (**f**) This yields a multi-exponential distribution of dwell times (black circles) to which we fit our kinetic model (red, see text, **Fig. 4a** and **Supplementary Fig. 4** for explanation).

Figure 3 The effect of Tus mutations on lock formation. (**a**) The Tus–*Ter* lock domain, depicted as a keyhole, forming a locked complex with either *TerB* (green key) or *TerB* with a mutated GC6 bp (magenta key). Wt Tus (purple) and *TerB* are a perfect match, H144A (blue) is a mutation deep within the lock (blue, cavity behind keyhole becomes larger), F140A is a mutation at the edge of the lock pocket (orange, keyhole becomes larger) and E49K is a mutation that lies close to the lock-domain (green, keyhole identical to wt). (**b**) The distribution of dwell times of wt Tus (purple, N = 94), the lock-domain mutants (H144A: blue, N = 642, F140A: orange, N = 344; E49K: green, N = 323) and binding domain mutant Q250A (cyan, N = 90) when bound to *TerB* at 59 pN (circles are binned data, solid lines are fits). (**c**) The force-dependent lifetimes of the eight lock domain investigations depicted in (**a**), as well as those of Q250A (cyan) and wt Tus in the permissive orientation (purple square). Shown is the lifetime of the longest-lived exponential (see **Supplementary Table 1** for other lifetimes); solid lines and circles are trends with *TerB*, while dashed lines and triangles are with mutated *TerB.* Error bars indicate the 1-σ confidence interval (CI). (**d**) The probability of entering the third, full lock state (same color scheme as (**c**). Error bars indicate the 1-σ CI). (**e**) The state-associated probabilities extracted (supplementary equations 1–4, **Supplementary Table 2**) for all Tus species on *TerB* at 59 pN (purple, cyan, green, orange and blue bars respectively represent wt, Q250A, E49K, F140A and H144A. Error bars represent the 1-σ CI).

Figure 4 Modeling Tus–*Ter* lock formation and extracting state-associated rates and probabilities. (**a**) State probabilities extracted through fitting the dwell time distributions at 59 pN for wt Tus–*Ter* (purple, same data as **Fig. 3e**) and wt Tus on the *Ter* site containing the mismatched bases 3–7 (yellow). The inset shows the force-extension curves of both types of hairpins, where the force at which the hairpin returns to its fully closed state consistently lies in the entropic regime (i.e., the forces at which ssDNA is no longer fully stretched) for the mismatch hairpin (yellow arrow, ~7 pN), while for the normal hairpin the closing force lies significantly higher (purple arrow, ~13 pN). (**b**) Fitting our 3-state exponential model (**Supplementary Fig. 4**) to the datasets allowed us to extract the kinetic rates (**c**) associated with the observed exponential states (**Supplementary equations 5–7**, **Supplementary Table 2**). We observed an exponential increase in all state exit rates (k_{10}, k_{20}, k_{30}; yellow, orange and red, respectively) with increasing force, while the rates connecting

states 1 and 2 (cyan) as well as states 2 and 3 (cyan, fill) remain roughly constant (error bars indicate 1-σ confidence intervals).

ONLINE METHODS

DNA hairpins. Plasmids pTER and pTER_Rev, containing the *TerB* site in either the non-permissive or permissive orientation respectively, and flanked by phage λ sequences, were obtained from Invitrogen. Plasmid pTER_mutant (*TerB*-C^6>G) was generated from pTER by site-directed mutagenesis using primers 1 and 2 (primer sequences are in **Table 1**). Hairpins were constructed in a multi-step process (**Supplementary Fig. 1**). First, 1 kb fragments containing the *TerB* site were amplified from the three pTER plasmids using primers 3 and 4 (**Table 1**). These fragments were digested with the non-palindromic restriction enzyme *Bsa*I (New England Biolabs inc., Ipswich, MA.) and ligated at one end with a 42-bp oligonucleotide to form a U-turn (oligonucleotide 5, **Table 1**). To create a 1-kb fragment containing a 5-base mismatch between bases 3–7 in the *Ter* site, two fragments of 500 bp were generated by PCR using pTER as template and primer combinations 3/12 and 4/13 respectively. These fragments were digested with *Bsa*I and ligated to each end of the annealed primer pair 14 and 15 containing the wobble. Hairpin handles were created by PCR amplification of a 1.2 kb pBluescript SK+ (Stratagene/Agilent Technologies, Santa Clara, CA) fragment using primers 6 and 7 (**Table 1**) in the presence of either biotin-16-dUTP or digoxigenin-11-dUTP (Roche Diagnostics, Basel, Switzerland). Prior to ligation to spacer oligonucleotides, handles were digested with either *Bam*HI or *Not*I. The upper spacer of the hairpin was generated by annealing 5'-phosphorylated oligonucleotides 8 and 9 (**Table 1**) and ligating this double stranded DNA fragment to the *Not*I-digested biotin-labelled handle. The lower spacer was made by annealing 5'-phosphorylated primers 10 and 11 (**Table 1**) and ligating them to the *Bam*HI-digested digoxigenin-labeled handle. Finally, the overhangs of these handle/spacer constructs were allowed to anneal to form a short (50-bp) stem with a 5'-GCAA overhang that was ligated to the complementary *Bsa*I site of the 1 kb *TerB* fragment. Oligonucleotides were obtained from Biolegio B.V., Nijmegen, the Netherlands and from Ella Biotech GmbH, Martinsried, Germany.

Table 1. Sequences of primers for PCR amplifications and oligonucleotides that contribute to the structure of the hairpin.

Oligonucleotide	Sequence
1	5'CACCACGACTGTGCTATAAAATAACTATGTTGTAACTAAAGTGGTTAATAT3'
2	5'ATATTAACCACTTTAGTTACAACATAGTTATTTTATAGCACAGTCGTGGTG3'
3	5'CTGCGGTCTCGTTGCTTACCGTCACCAGAAATTACCGTCAC3'
4	5'CCATCTTGGTCTCCTAGGTTTTTAGCAGCGAAGCGTTTGATAAG3'
5	5'CCTAAGCTCGCCGAGGCGAGCGAAAGCTCGCCTCGGCGAGCT3'

6	5'GACCGAGATAGGGTTGAGTG3'
7	5'CAGGGTCGGAACAGGAGAGC3'
8	5'GGCAAGAGCAACTCGGTCGCCGCATACACTATTCTCAGAATGACTTGGTT3'
9	5'GGCCAACCAAGTCATTCTGAGAATAGTGTATGCGGCGACCGAGTTGCTCTTGCCATGCTCTTTA CAACCGGTTGACTGCTTCAGGGGTCGATCCCGCTTTGTAC3'
10	5'GATCTCGTTCATCCATAGTTGCCTGACTCCCCGTCGTGTAGATAACTACGATACGGGAGGGCTT ACCATCTGGC3'
11	5'GCAAGTACAAAGCGGGATCGACCCCTGAAGCAGTCAACCGGTTGTAAAGAGCATCGATCGTT GTCAGAAGTAAGTTGGCCGCAGTGTTATCACTCATGGTTATGCCAGATGGTAAGCCCTCCCGTAT CGTAGTTATCTACACGACGGGGAGTCAGGCAACTATGGATGAACGA3'
12	5'CCATCTTGGTCTCCGACATTATAGCACAGTCGTGGTGAC3'
13	5'CTGCGGTCTCGAGGCGGTTAATATTATGGCGCGTTG3'
14	5'P-GCCTACTTTAGTTACAACATACTTATT3'
15	5'P-TGTCAAACCTCATGTTGTAACTAAAGT3'

Tus proteins. N-terminally His_6-tagged Tus and mutant derivatives were prepared as described[21,22]; their concentrations were determined spectrophotometrically (ε_{280} = 39,700 $M^{-1}cm^{-1}$).

Magnetic tweezers – experimental configuration. The magnetic tweezers implementation used in this study has been described[30,31,37]. In short, light transmitted through the sample was collected by an oil-immersion objective (Olympus UPLSAPO60XO 60X, NA = 1.35, Olympus, USA) and projected onto a 12 MP CMOS camera (Falcon FA-80-12M1H, Teledyne Dalsa, Canada) with a sampling frequency of 58 Hz at full field of view, or higher when cropped. A 2 inch 200 mm tube lens between objective and camera made the effective magnification 67X. The applied magnetic field was generated by a pair of vertically aligned permanent neodymium-iron-boron magnets (SuperMagnete, Switzerland) separated by a distance of 1.0 or 0.5 mm, suspended on a motorized stage (M-126.PD2, Physik Instrumente, Germany) above the flow cell. Additionally, the magnet pair could be rotated about the illumination axis by an applied DC servo step motor (C-150.PD, Physik Instrumente, Germany).

Data processing. Image processing of the collected light was used to track the real-time position of both surface-attached reference beads and superparamagnetic beads coupled to DNA tethers in three dimensions. We implemented custom written software in C++, CUDA and LabView (2011, National Instruments Corporation, USA) that is suited for high-throughput tracking in magnetic tweezers[37]. In short, tracking of the *x*,*y* coordinates is performed using center-of-mass computation followed by a further refinement using the quadrant interpolation algorithm. Localization of the bead's *z*-coordinate is achieved by creating a radial profile using the refined *x*,*y* coordinates and comparing this profile to a pre-recorded LUT of radial profiles. After subtraction of the reference bead position to correct for instrumental drift, the *x*, *y* and *z* positions of the DNA-tethered beads were determined with a spatial accuracy of <3 nm. The upward stretching forces on the DNA tethers by the superparamagnetic beads were calibrated from analysis of the

extent of its Brownian motion, whereby spectral corrections were employed to correct for camera blur and aliasing[38,39].

Sample preparation and data acquisition. The sample preparation used in this study has been described in detail elsewhere[31]. In short, the DNA hairpins (final concentration ~50 pg/µl) were mixed and incubated for 2 min with 20 µl streptavidin-coated paramagnetic polystyrole beads (M270 Dynabeads) at room temperature in TRIS buffer (50 mM Tris-HCl pH 7.9, 50 mM KCl, 0.1 mM EDTA, 0.01% Triton X-100). The supernatant was replaced by 50 µl TRIS buffer followed by a 15 min incubation of the bead-DNA solution in the flow cell containing an anti-digoxigenin-coated nitrocellulose surface. Non-tethered beads were removed by flushing with 1 ml TRIS buffer, applying a high (30–40 pN) force while rotating the magnets (10 rpm), followed by flushing with more buffer until all non-tethered beads had been flushed out. All KCl buffers used in this study exclusively contained 50 mM Tris-HCl pH 7.9, 0.1 mM EDTA, 0.01% Triton X-100 unless noted otherwise. Tus proteins were diluted 10^3-fold from stock (to ~10 nM) unless high salt concentrations required higher concentrations. Data were acquired at 100 Hz, 10 ms acquisition time. Force-extension curves were obtained through changing the magnet position in an exponential fashion such that the force change was linear. Constant-force dwell time experiments were obtained by lowering the magnets in a linear fashion (10 mm/s) to the desired distance. The dwell time is the time measured between arrival of the magnets at their final position and the further opening of the hairpin from the locked to the fully opened state.

Data analysis and statistical procedure. Rupture of the Tus–*Ter* lock results in a sudden opening of the DNA hairpin: rupture points are easily identified as a sharp peak in the derivative of the z-trace. The dwell-time distribution

$$P(t) = \sum_{i=1}^{N} A_i e^{-k_i t} \qquad (1)$$

with *M* number of exponentials (as determined by the Bayes–Schwartz information criterion[27]) is fit to the dataset containing *N* experimentally collected dwell times $\{\tau_i\}_i$ by minimizing the likelihood function[28]

$$L = -\sum_{i}^{N} \ln P(t_i) \qquad (2)$$

with respect to rates and probabilistic weights (**Supplementary Eqns. 2-3**). We calculate the errors in our parameter estimates by bootstrapping the system 1000 times, and report the one-sigma confidence intervals (1-σ CI) among the bootstrapped data sets (**Supplementary Tables 1 and 2**).

REFERENCE LIST

1. Hill, T.M., Henson, J.M. & Kuempel, P.L. The terminus region of the *E. coli* chromosome contains two separate loci that exhibit polar inhibition of replication. *Proc. Natl. Acad. Sci. USA*, **84**, 1754–1758 (1987).
2. Hidaka, M., Kobayashi, T., Takenaka, S., Takeya, H. & Horiuchi, T. Purification of a DNA replication terminus (ter) site-binding protein in *Escherichia coli* and identification of the structural gene. *J. Biol. Chem.* **264**, 21031–21037 (1989).
3. Hill, T. M. Arrest of bacterial DNA replication. *Annu. Rev. Microbiol.*, **46**, 603–633 (1992).
4. Kamada, K., Horiuchi, T., Ohsumi, K., Shimamoto, N. & Morikawa, K. Structure of a replication-terminator protein complexed with DNA. *Nature* **383**, 598–603 (1996).
5. Khatri G.S., MacAllister T., Sista P.R. & Bastia D. The replication terminator protein of *E. coli* is a DNA sequence-specific contra-helicase. *Cell* **59,** 667–674 (1989).
6. Hill, T.M. & Marians K.J. *Escherichia coli* Tus protein acts to arrest the progression of DNA replication forks *in vitro*. *Proc. Natl. Acad. Sci. USA* **87**, 2481–2485 (1990).
7. Hill, T. M. Features of the chromosomal terminus region, p. 1602–1614. In F.C. Neidhardt *et al.* (ed.), *Escherichia coli* and *Salmonella*: Cellular and Molecular Biology, 2nd ed., vol. 2. American Society for Microbiology, Washington, D.C. (1996).
8. Coskun-Ari, F.F., Skokotas, A., Moe, G.R. & Hill, T.M. Biophysical characteristics of Tus, the replication arrest protein of *Escherichia coli*. *J. Biol. Chem.* **269**, 4027–4034 (1994).
9. Neylon, C., Kralicek, A.V., Hill, T.M. & Dixon, N.E. Replication termination in *Escherichia coli*: structure and anti-helicase activity of the Tus-*Ter* complex. *Microbiol. Mol. Biol. Rev.* **69**, 501–526 (2005).
10. Lee, J.Y., Finkelstein, I.J., Arciszewska, L.K., Sherratt, D.J. & Greene E.C. Single-molecule imaging of FtsK translocation reveals mechanistic features of protein-protein collisions on DNA. *Mol. Cell* **54**, 832–843 (2014).
11. Kaul, S. *et al.* The replication terminator protein of the gram-positive bacterium *Bacillus subtilis* functions as a polar contrahelicase in gram-negative *Escherichia coli*. *Proc. Natl. Acad. Sci. USA* **91**, 11143–11147 (1994).
12. Andersen, P.A., Griffiths, A.A., Duggin, I.G. & Wake, R.G. Functional specificity of the replication fork-arrest complexes of *Bacillus subtilis* and *Escherichia coli*: significant specificity of Tus-*Ter* functioning in *E. coli*. *Mol. Microbiol.* **36,** 1327–1335 (2000).
13. Sahoo, T., Mohanty, B.K., Lobert, M., Manna, A.C. & Bastia, D. The contrahelicase activities of the replication terminator proteins of *Escherichia coli* and *Bacillus subtilis* are helicase-specific and impede both helicase translocation and authentic DNA unwinding. *J. Biol. Chem.* **270**, 29138–29144 (1995).
14. Mulugu, S. *et al.* Mechanism of termination of DNA replication of *Escherichia coli* involves helicase-contrahelicase interaction. *Proc. Natl. Acad. Sci. USA* **98**, 9569–9574 (2001).
15. Mohanty B.K., Sahoo T. & Bastia D. The relationship between sequence-specific termination of DNA replication and transcription. *EMBO J.* **15**, 2530 –2539 (1996).
16. Mohanty, B.K., Sahoo, T., & Bastia, D. Mechanistic studies on the impact of transcription on sequence-specific termination of DNA replication and vice versa. *J. Biol. Chem.* **273**, 3051–3059 (1998).
17. Lee, E.H., Kornberg, A., Hidaka, M., Kobayashi, T. & Horiuchi, T. *Escherichia coli* replication termination protein impedes the action of helicases. *Proc. Natl. Acad. Sci. USA* **86**, 9104 –9108 (1989).
18. Lee, E.H., & Kornberg, A. Features of replication fork blockage by the *Escherichia coli* terminus-

binding protein. *J. Biol. Chem.* **267**, 8778–8784 (1992).
19. Bedrosian, C.L. & Bastia, D. *Escherichia coli* replication terminator protein impedes simian virus 40 (SV40) DNA replication fork movement and SV40 large tumor antigen helicase activity *in vitro* at a prokaryotic terminus sequence. *Proc. Natl. Acad. Sci. USA* **88**, 2618–2622 (1991).
20. Hidaka, M. *et al.* Termination complex in *Escherichia coli* inhibits SV40 DNA replication in vitro by impeding the action of T antigen helicase. *J. Biol. Chem.* **267**, 5361–5365 (1992).
21. Mulcair, M.D. *et al.* A molecular mousetrap determines polarity of termination of DNA replication in *E. coli*. *Cell*, **125**, 1309–1319 (2006).
22. Neylon, C., *et al.* Interaction of the *Escherichia coli* replication terminator protein (Tus) with DNA: a model derived from DNA-binding studies of mutant proteins by surface plasmon resonance. *Biochemistry* **39**, 11989–11999 (2000).
23. Bastia, D. *et al.* Replication termination mechanism as revealed by Tus-mediated polar arrest of a sliding helicase. *Proc. Natl. Acad. Sci. USA* **105**, 12831–12836 (2008).
24. Liphardt, J., Onoa, B., Smith, S.B., Tinoco, I. Jr. & Bustamente, C. Reversible unfolding of single RNA molecules by mechanical force. *Science* **292**, 733–737 (2001).
25. Woodside, M.T. *et al.* Nanomechanical measurements of the sequence-dependent folding landscapes of nucleic acid hairpins. *Science* **103**, 1690–1695 (2006).
26. Lionnet, T., Spiering, M.M., Benkovic, S.J., Bensimon, D. & Croquette, V. Real-time observation of bacteriophage T4 gp41 helicase reveals an unwinding mechanism. *Proc. Natl. Acad. Sci. USA* **104**, 19790–19795 (2007).
27. Schwarz, G. Estimating dimension of a model. *Ann. Stat.* **6**(2), 461–464 (1978).
28. Cowan, G. Statistical Data Analysis, Oxford University Press, Oxford, U.K. (1998).
29. Press, W.H., Flannery, B.P., Teukolsky, S.A. & Vetterling, W.T. Numerical recipes in C: the art of scientific computing. Cambridge University Press, Cambridge, U.K. (1992).
30. Dulin, D. *et al.* Elongation-competent pauses govern the fidelity of a viral RNA-dependent RNA polymerase. *Cell Reports* **10**, 983–992 (2015).
31. Janissen, R. *et al.* Invincible DNA tethers: covalent DNA anchoring for enhanced temporal and force stability in magnetic tweezers experiments. *Nucleic Acids Res.* **42**, e137 (2014).
32. Coskun-Ari, F.F., Hill, T.M. Sequence-specific interactions in the Tus–*Ter* complex and the effect of base pair substitutions on arrest of DNA replication in Escherichia coli. *J. Biol. Chem.* **272**, 26448–26456 (1997).
33. Dantus, M., Bowman, R.M., Zewail, A.H. Femtosecond laser observations of molecular vibration and rotation. *Nature* **343**, 737–739 (1990).
34. Arasaki, Y., Takatsuka, K., Wang, K., McKoy, V. Energy- and angle-resolved pump-probe femtosecond photoelectron spectroscopy: Molecular rotation. *J. Chem. Phys.* **114**, 7941–7950 (2001).
35. Middleton, C.T., De La Harpe, K., Su, C., Law, Y-K., Crespo-Hernández, C.E., Kohler, B. DNA excited-state dynamics: from single bases to the double helix. *Annu. Rev. Phys. Chem.* **60**, 217–239 (2009).
36. Tome, J.M. *et al.* Comprehensive analysis of RNA-protein interactions by high-throughput sequencing–RNA affinity profiling. *Nat. Meth.* **11**, 683–688 (2014).
37. Cnossen, J.P., Dulin, D., Dekker, N.H. An optimized software framework for real-time, high-throughput tracking of spherical beads. *Rev. Sci. Instrum.* **85**, 103712 (2014).
38. Te Velthuis, A.J., Kerssemakers, J.W., Lipfert, J. and Dekker, N.H. Quantitative guidelines for force calibration through spectral analysis of magnetic tweezers data. *Biophys. J.* **99**, 1292–1302 (2010).
39. Yu, Z. *et al.* A force calibration standard for magnetic tweezers. *Rev. Sci. Instrum.* **85**, 123114 (2014).

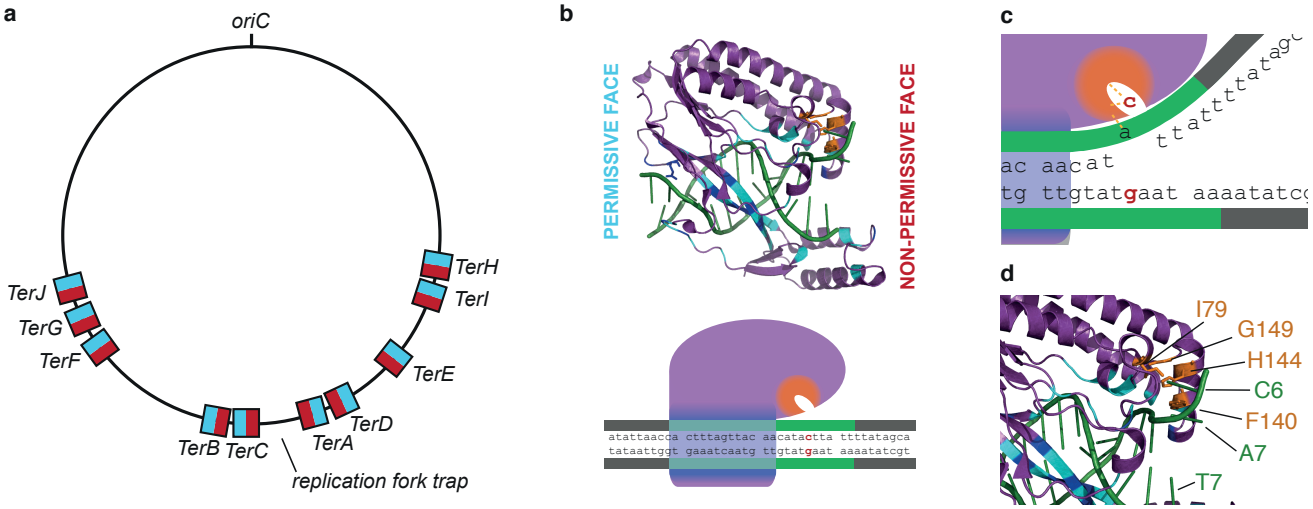

Figure 1

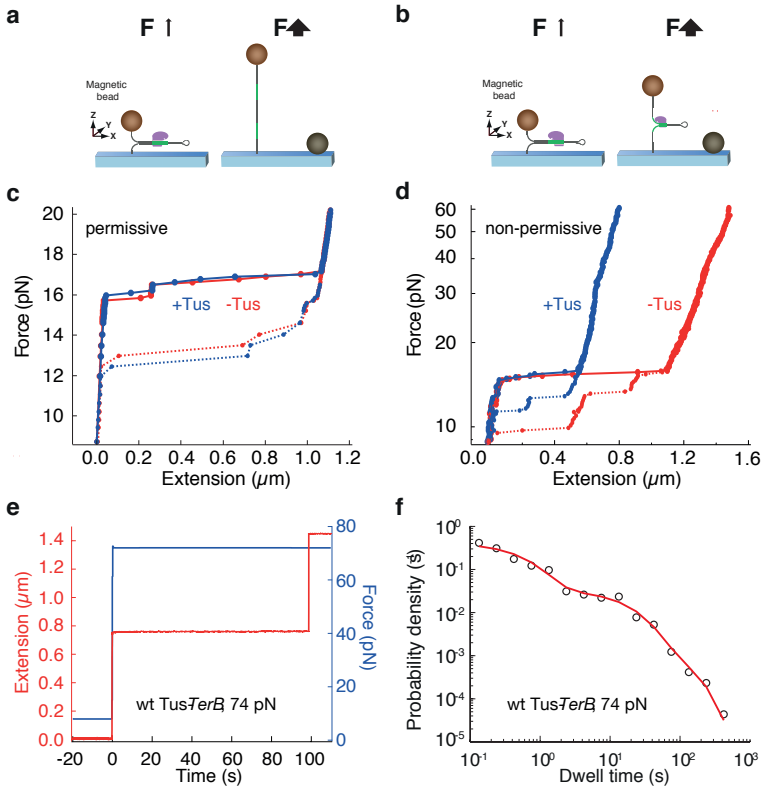

Figure 2

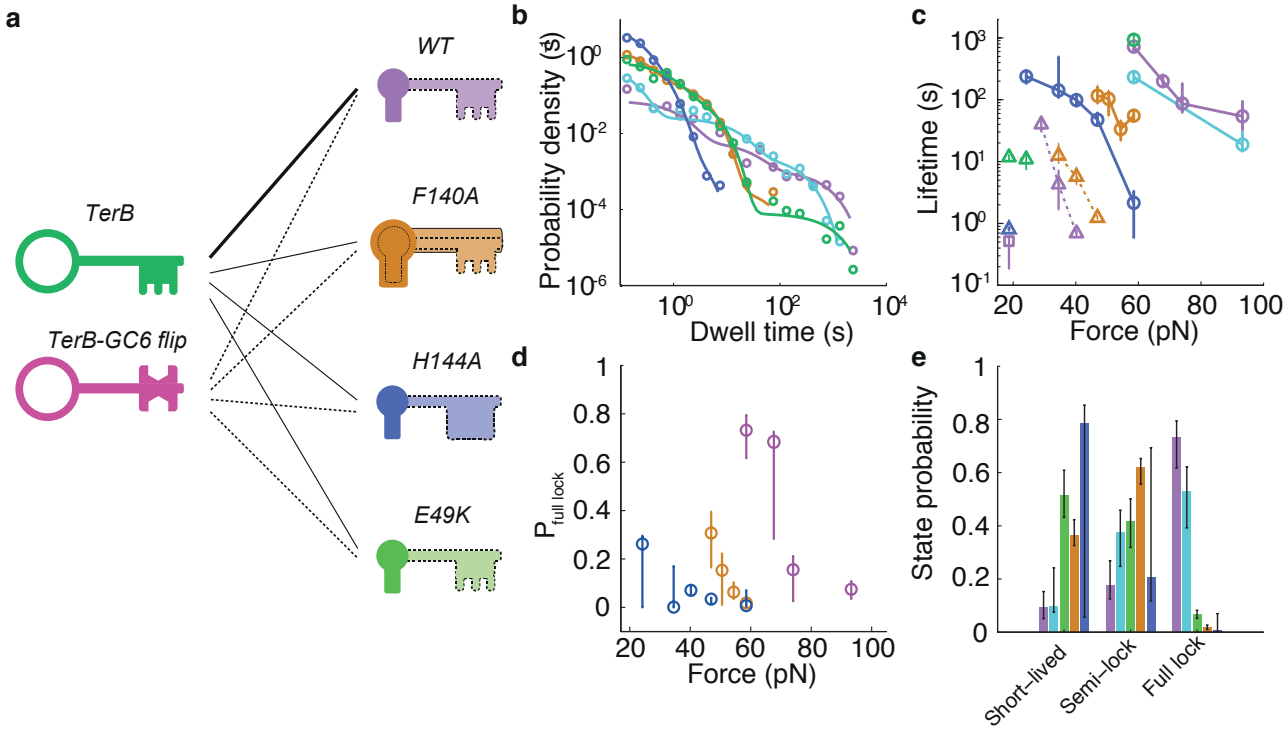

Figure 3

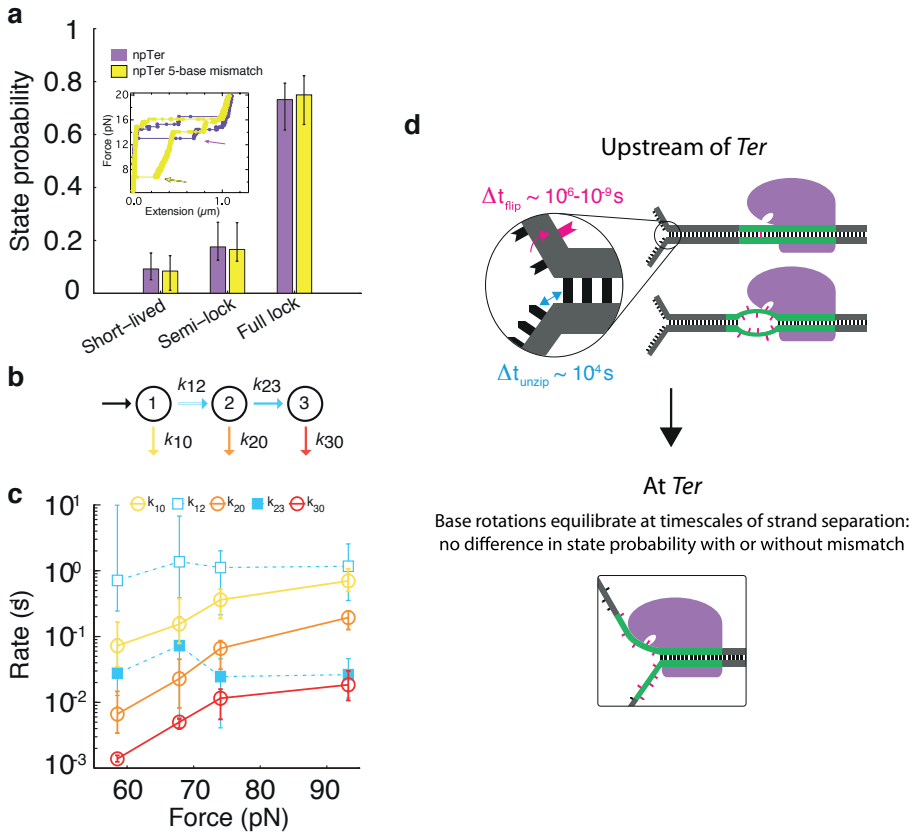

Figure 4

Supplementary Information for:

Strand separation establishes a sustained lock at the Tus–*Ter* replication fork barrier

Bojk A. Berghuis[1], David Dulin[1], Zhi-Qiang Xu[2], Theo van Laar[1], Bronwen Cross[1], Richard Janissen[1], Slobodan Jergic[2], Nicholas E. Dixon[2], Martin Depken[1] & Nynke H. Dekker[1*]

[1]Department of Bionanoscience, Kavli institute of Nanoscience, Delft University of Technology, Lorentzweg 1, 2628 CJ Delft, The Netherlands

[2]Centre for Medical and Molecular Bioscience and School of Chemistry, University of Wollongong, New South Wales 2522, Australia

* Correspondence may be addressed to n.h.dekker@tudelft.nl.

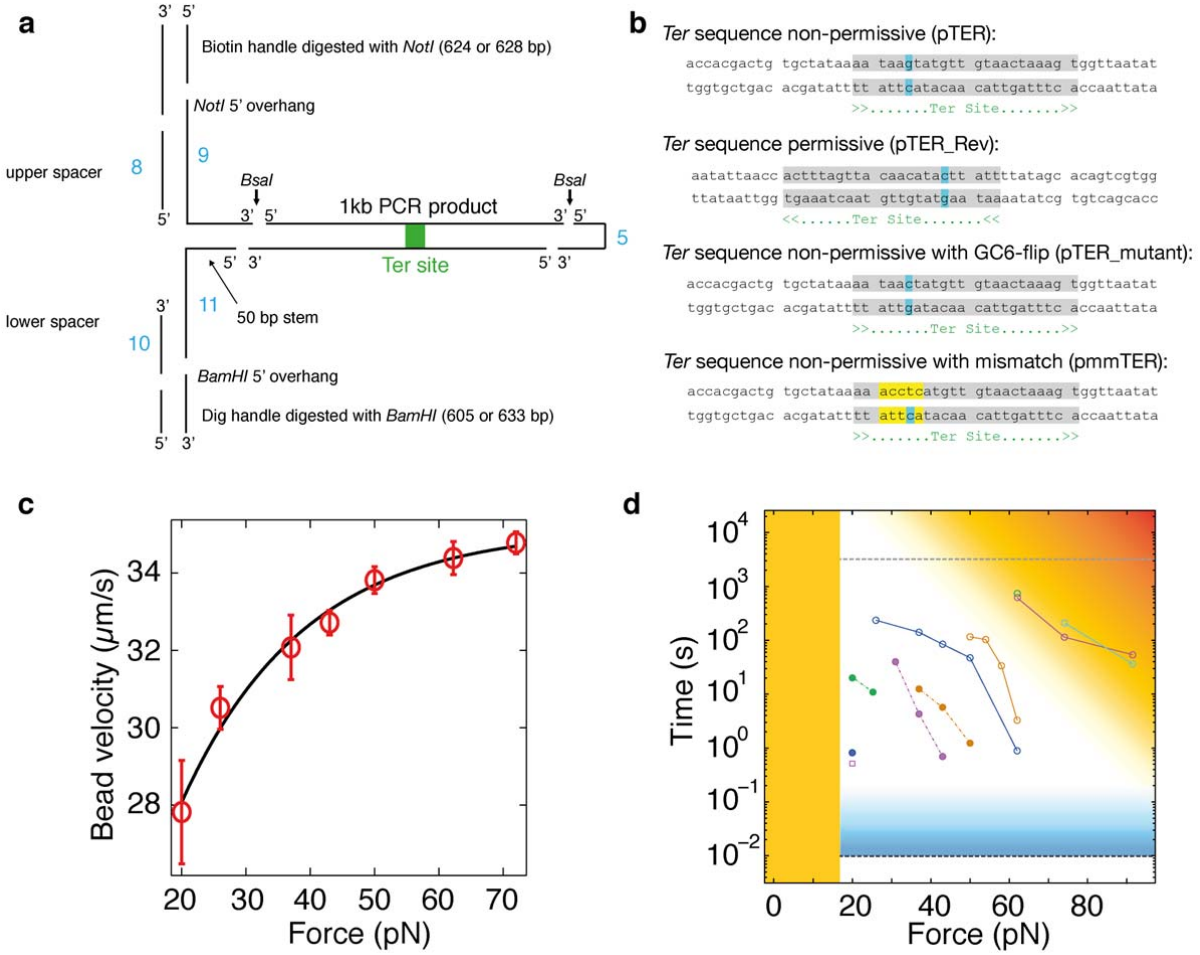

Figure 1. DNA hairpin design and characteristics. **(a)** The DNA hairpin construct made as described in the **Online Methods**. (**b**) The used *Ter* sequences. **(c)** Velocity versus force profile of a hairpin opening in the magnetic tweezers. We compute velocities by determining the maximum value of the central derivative of the extension versus time traces, i.e. the instantaneous apparent velocity upon lock rupture. Each data point in the figure is the average of hundreds of rupture events (the data here are from ~10^4 rupture events). The

data have been fit with a single exponential (black line) to provide a guide to the eye. Note that our computations only provide a lower bound to the velocity, since our 100 Hz sampling frequency is not sufficiently high to capture the opening dynamics over a typical distance of ~0.6 µm (500 bp opening). Nonetheless, these lower bounds suffice to indicate that the hairpin-opening rate exceeds the DNA unwinding rate of the *E. coli* replisome by at least 10-fold at 20 pN force. **(d)** Here we visualize the constraints on the experimental time–force window due to biological (orange) or instrumentation (blue) limits. The data, identical to Figure 3c, is added as a frame of reference. Below ~16 pN, base-paired DNA is energetically more favorable, therefore the hairpin remains closed (orange fill). With an acquisition rate of 100 Hz, the cutoff time is in principle 10^{-2} s (black dashed line); however, the error already becomes relatively large for lock lifetimes shorter than 0.1 s (blue gradient). Measurements are further limited by the lifetime of the DNA hairpin since DNA tethering relies on electrostatic interactions. This implies that very long measurement times, high forces or a combination of both (orange gradient) should be avoided. Typically we avoided having to measure lifetimes exceeding an hour (grey dashed line). Here we are able to see that the force–lifetime behavior exhibited by wt Tus already approaches the limits of the assay.

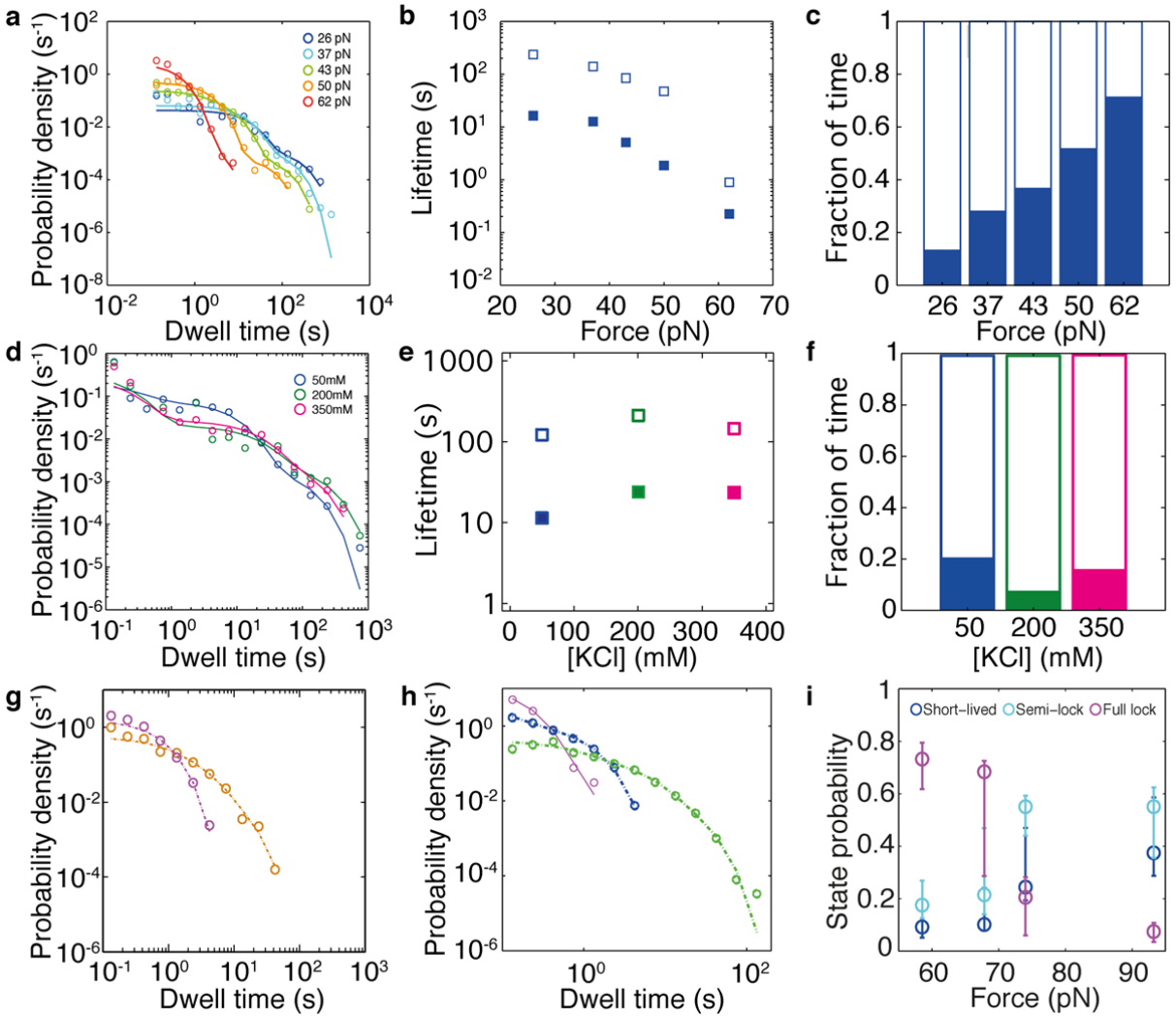

Figure 2. Extended characteristics of Tus–*Ter* force-dependent lifetimes. Distribution of lock lifetimes with varying force (**a**–**c**) or KCl concentration (**d**–**f**, see text below). The force-dependency was acquired with H144A Tus–*TerB* at 50 mM KCl, and the salt-dependency was acquired with wt Tus–*TerB* at 74 pN. (**a**, **d**) Probability densities (circles) including fits (solid lines). (**b**, **e**) The two longest-lived lifetimes extracted through fitting all datasets (filled squares are the second intermediate state, open squares represent the full lock state). (**c**, **f**) The normalized contribution of each of the fit states to the total experimental time (filled bar is the second state, open bar the full lock state). (**g, h**) Lifetime distributions obtained for the *TerB* GC flipped mutant and permissive orientation. (**g**) Fit probability density distributions of wt Tus and F140A with the GC-flipped *TerB* sequence at 40 pN (purple and orange, respectively). (**h**) Fit probability density distributions of bound-only wt Tus (i.e. in the permissive orientation, purple circles and solid line), H144A combined with the GC flipped *Ter* (blue), and E49K (green) with the GC flipped *Ter* at 19 pN. The lines represent fits to the data. (**i**) Trends in probabilities of all 3 lock states obtained through fitting our 3-state model to the wt Tus–*Ter* dataset.

Salt-dependence of Tus–*Ter* lock

As the reported dissociation constant (K_D) of the Tus–ds*TerB* complex has been shown to be highly salt-dependent, we investigated whether *lock formation* also exhibits a strong salt dependence. We observed that the fraction of rupture events recorded with a lifetime below our cutoff time of 10^{-2} s (i.e., the fraction of open hairpins at t = 0 s) increased from 0% at 50 mM to 14% at 350 mM KCl, while during these experiments care was taken to keep [Tus] well above (at least an order of magnitude) the reported salt-dependent K_D, thereby ensuring the continuous binding of Tus to *Ter*. Concomitantly, we observed that the lifetimes of the two longest-lived exponentials for wt Tus remain virtually unaffected when increasing the [KCl] from 50 to 350 mM, indicating that the lock *strength* is hardly affected by salt concentration (**Supplementary Fig. 2d–f**). In contrast, the reported K_D of the Tus–ds*TerB* complex increases from ~10^{-13} to ~10^{-8} M within the 50 to 350 mM range. We conclude from this that the rate of lock formation is slightly affected by ionic screening, but once the lock is formed its strength remains unaffected. This is in accord with SPR data.

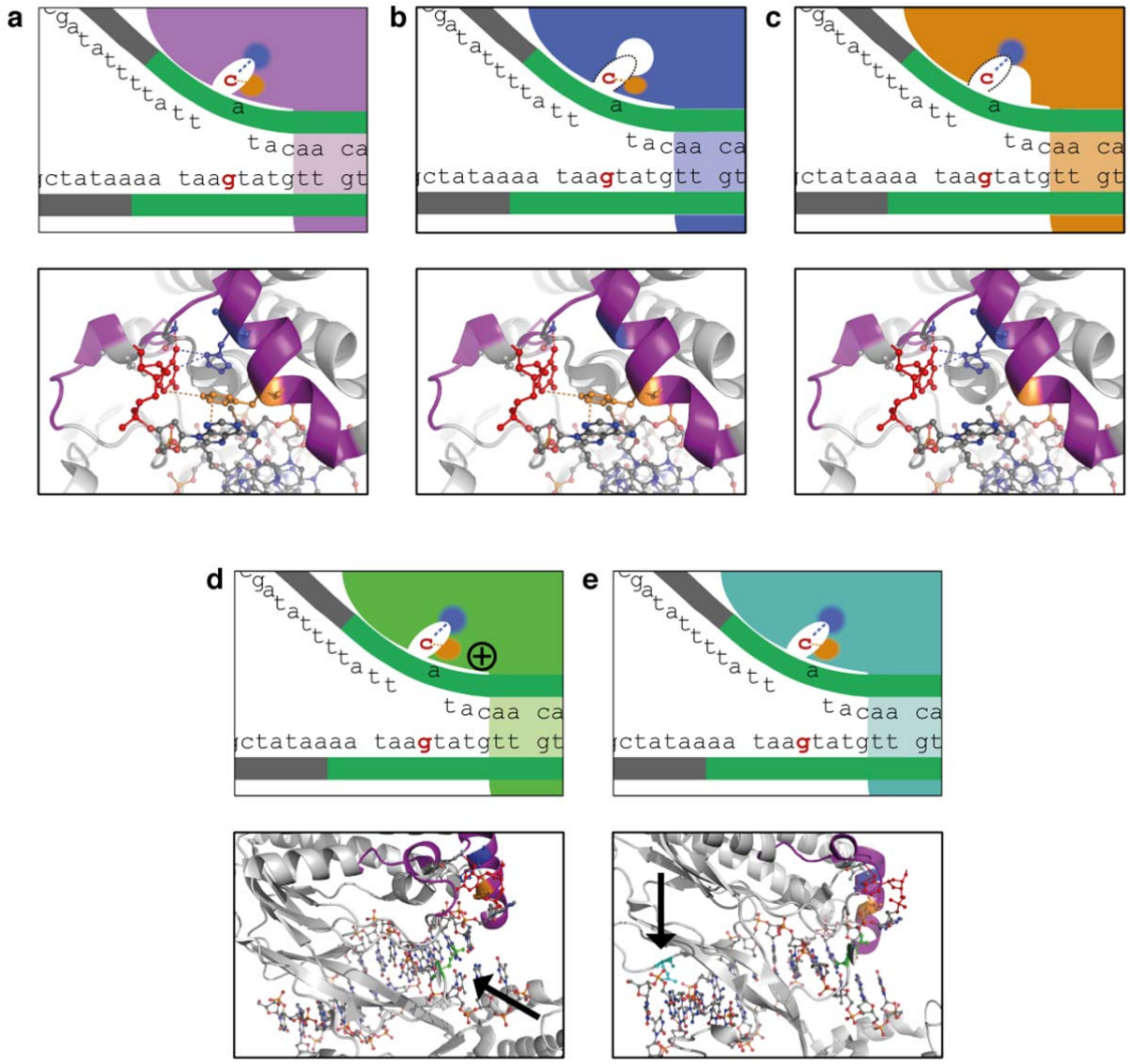

Figure 3. Schematic representations of Tus mutations and the corresponding domains in the crystal structure. Shown is the schematic representation of the lock domain of wt Tus (**a**, purple), inner lock domain mutant H144A (**b**, blue), edge lock domain mutant F140A (**c**, orange), outside lock domain mutant E49K (**d**, green) and binding domain mutant Q250A (**e**, cyan), as well as the relevant areas of the crystal structure directly below. Shown is how the C6 base (red) interacts with various amino acids of the lock domain (purple cartoon representation). Since amino acids E49 and Q250 are not part of the lock pocket both amino acids are indicated with an arrow.

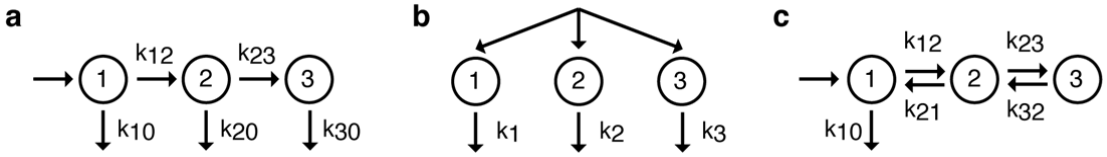

Figure 4. Kinetic models that could fit the lifetime distributions. Although there are many different three-state models that can fit our data, we have good reason to assume that our sequential model (**a**) is the simplest that can explain it. We consider it more likely that these substructures are on-pathway intermediate states towards a fully locked state instead of three completely independent structures induced by our pulling experiments, as explained in the Discussion section of the main manuscript. By extracting the rates we find that only the exit rates show a dependence on force (**Main Text Fig. 4b,c**). Interestingly, the inter-state rates (k_{12} and k_{23}) are shielded from the force we subject the Tus–*Ter* system to in our assay. The fact that we observe an exponential dependency on force of only the off-rates implies that the force dependency of the probabilities (supplementary eqns. 4–7) and lifetimes we observe only depend on the state exit rates. **Table 2** contains all the rates of the datasets presented in this work. Depending on the outcome of the Bayes-Schwartz information criterion, either a two or three exponential fit was used. (**b**) If sequential, progressive strengthening of states were not the case, a model with 3 independent states can also fit the data, yielding probabilities (the A's in **Table 1**) very similar to those obtained by fitting our sequential model (P's in **Table 2**). However, now all the parameters of this model display force-dependent trends, as we show that both the state lifetimes as well as the rates underlying the probabilities are force-dependent (**Fig. 2a–c** and **Main Text Fig. 3d**, respectively). (**c**) While there are many more three-state models that can fit our data, all add an additional complexity that cannot be verified by our experiments. This also holds true in the case of the reverse-exit model shown here. But since we are applying large forces to the system, we might modify the exit pathway out of the Tus–*Ter* lock state. While *in vivo* there might be a reverse order of exiting, our high pulling forces likely deform the energy landscape in such a way that other exit pathways also become available. Intuitively this makes sense since reverse exit implies a return of the *Ter* bases at the fork to their base-paired conformation – the forces applied in our experiments will always prevent this from happening.

Table 1. The fit parameters to generate the fits (k1–3 and A1-3, equation (1)) as well as the lifetimes associated with each state (τ1-3; the inverse of the respective *k*s). Lower and upper 1-σ CIs are shown left and right below each value respectively.

Dataset	k1 (1/s)	k2 (1/s)	k3 (1/s)	A1	A2	A3	τ1 (s)	τ2 (s)	τ3 (s)
E49K 50mM 59 pN	1.3974	0.2432	0.0011	0.4254	0.5055	0.0691	0.72	4.11	932.63
	1.0512 1.8991	0.2062 0.2793	0.0009 0.0013	0.3463 0.5354	0.3969 0.5865	0.0521 0.0831	0.53 0.95	3.58 4.85	772.62 1097.00
E49KGCf 50mM 19 pN	1.3655	0.2237	0.0646	0.1912	0.5535	0.2554	0.73	4.47	15.47
	0.7784 2.0261	0.1411 0.3062	0.0430 0.0774	0.1253 0.3331	0.4822 0.6200	0.0898 0.3741	0.49 1.28	3.27 7.09	12.92 23.24
E49KGCf 50mM 24 pN	1.7844	0.4405	0.0519	0.9070	0.0748	0.0182	0.56	2.27	19.26
	1.7052 2.0610	0.3415 1.5680	0.0368 0.0919	0.0007 0.9301	0.0543 0.9410	0.0103 0.0348	0.49 0.59	0.64 2.93	10.88 27.16
F140A 50mM 47 pN	7.3335	0.0731	0.0086	0.3966	0.2549	0.3486	0.14	13.68	116.29
	5.9305 12.7417	0.0404 0.3144	0.0060 0.0116	0.3340 0.5092	0.1442 0.3839	0.1902 0.4282	0.08 0.17	3.18 24.75	85.93 167.64
F140A 50mM 50 pN	1.6428	0.0536	0.0097	0.2275	0.5843	0.1882	0.61	18.67	103.08
	1.2645 73.4507	0.0457 0.1169	0.0072 0.0183	0.1837 0.9808	0.0085 0.6500	0.0096 0.2821	0.01 0.79	8.55 21.89	54.65 139.58
F140A 50mM 54 pN	19.6676	0.1630	0.0298	0.3799	0.5430	0.0771	0.05	6.13	33.61
	9.8855 31.1323	0.1476 0.1933	0.0214 0.0463	0.2361 0.6245	0.3010 0.6643	0.0391 0.1347	0.03 0.10	5.17 6.77	21.61 46.62
F140A 50mM 59 pN	4.7211	0.3507	0.0181	0.3139	0.6671	0.0190	0.21	2.85	55.27
	3.4487 6.6327	0.3168 0.3873	0.0153 0.0216	0.2766 0.3735	0.6058 0.7035	0.0107 0.0287	0.15 0.29	2.58 3.16	46.34 65.34
F140AGCf 50mM 35 pN	0.5269	0.0799		0.5382	0.4618		1.90	12.52	
	0.3206 0.9963	0.0509 0.1070		0.3576 0.7469	0.2526 0.6421		1.00 3.12	9.35 19.63	
F140AGCf 50mM 40 pN	1.0714	0.1757		0.5317	0.4683		0.93	5.69	
	0.7378 2.8859	0.1340 0.2331		0.3418 0.6837	0.3163 0.6575		0.35 1.36	4.29 7.46	
F140AGCf 50mM 47 pN	6.1670	0.8115		0.2588	0.7412		0.16	1.23	
	5.1176 7.3741	0.7731 0.8504		0.2269 0.2986	0.7011 0.7725		0.14 0.20	1.18 1.29	
H144A 50mM 24 pN	14.9928	0.0579	0.0042	0.1094	0.6081	0.2825	0.07	17.29	238.43
	0.4369 100.0000	0.0428 0.0691	0.0034 0.0054	0.0725 0.9981	0.0013 0.6432	0.0005 0.3258	0.01 2.29	14.46 23.36	184.54 290.91
H144A 50mM 35 pN	100.0000	0.0779	0.0071	0.9952	0.0039	0.0009	0.01	12.84	141.63
	0.0897 100.0000	0.0137 0.0802	0.0020 0.0092	0.0778 0.9927	0.0057 0.7413	0.0016 0.1938	0.01 11.15	12.47 72.77	108.65 488.25
H144A 50mM 40 pN	0.9332	0.1513	0.0101	0.2001	0.7238	0.0761	1.07	6.61	98.74
	0.6735 14.1291	0.1363 0.1832	0.0087 0.0126	0.1235 0.3013	0.6263 0.7954	0.0572 0.0915	0.07 1.48	5.46 7.34	79.21 114.57
H144A 50mM 47 pN	99.0198	0.5380	0.0211	1.22E-04	0.9645	0.0354	0.01	1.86	47.42
	0.5996 100.0000	0.3750 0.5335	0.0164 0.0255	0.0009 0.9416	0.0481 0.9587	0.0195 0.0418	0.01 1.67	1.87 2.67	39.23 60.86
H144A 50mM 59 pN	6.0193	2.3191	0.4642	0.6550	0.3352	0.0098	0.17	0.43	2.15
	5.3403 99.7892	1.9081 4.5799	0.3036 1.6819	0.0009 0.7652	0.2067 0.7556	0.0037 0.1306	0.01 0.19	0.22 0.52	0.59 3.29
H144AGCf 50mM 19 pN	10.8718	1.2214		0.2124	0.7876		0.09	0.82	
	6.0554 31.3382	1.1389 1.2910		0.1901 0.5849	0.4051 0.8098		0.03 0.17	0.77 0.88	
Q250A 200mM 59pN	50.9000	0.0925	0.0046	0.8098	0.1540	0.0362	0.02	10.81	219.54
	4.5013 67.2385	0.0780 0.1032	0.0038 0.0057	0.4415 0.9364	0.0266 0.4545	0.0042 0.1344	0.01 0.22	9.69 12.82	176.19 262.00
Q250A 50mM 59 pN	7.6697	0.0657	0.0043	0.0928	0.3399	0.5673	0.13	15.23	232.29
	0.2996 10.6434	0.0302 0.1375	0.0035 0.0051	0.0720 0.2221	0.2205 0.4223	0.4427 0.6560	0.09 3.34	7.27 33.13	194.67 286.12
Q250A 50mM 93 pN	100.0000	0.7251	0.0530	0.9980	0.0016	0.0004	0.01	1.38	18.85
	0.9019 100.0000	0.1305 0.7635	0.0196 0.0675	0.3342 0.9985	0.0012 0.5328	0.0003 0.1073	0.01 1.11	1.31 7.67	14.82 50.97
WT 200mM 74 pN	13.7971	0.0486	0.0048	0.2245	0.3365	0.4390	0.07	20.56	206.86
	0.7918 25.0195	0.0252 0.2076	0.0036 0.0066	0.1212 0.4298	0.1575 0.4679	0.2483 0.5759	0.04 1.26	4.82 39.69	151.47 279.95
WT 200mM 93 pN	1.0919	0.1625	0.0311	0.4163	0.5291	0.0547	0.92	6.16	32.19
	0.9192 1.7879	0.1472 0.6839	0.0224 0.0957	0.2012 0.4782	0.4341 0.6032	0.0311 0.3634	0.56 1.09	1.46 6.79	10.45 44.71
WT 350mM 74 pN	12.6376	0.0469	0.0071	0.1848	0.4464	0.3687	0.08	21.31	140.11
	8.8062 17.8469	0.0395 0.0576	0.0063 0.0082	0.1076 0.3063	0.3402 0.5134	0.2751 0.4523	0.06 0.11	17.35 25.32	122.26 157.79
WT-mmTer 50mM 59 pN	0.3550	0.0247	0.0018	0.0998	0.2101	0.6900	2.82	40.51	541.90
	0.1608 3.3106	0.0098 0.0909	0.0017 0.0021	0.0250 0.1608	0.1529 0.3477	0.5258 0.7925	0.30 6.22	11.00 101.61	481.12 600.87
WT 50mM 59 pN	0.7843	0.0343	0.0014	0.0843	0.1514	0.7643	1.27	29.16	720.22
	0.2804 16.0718	0.0175 0.1149	0.0012 0.0016	0.0454 0.1429	0.1021 0.2301	0.6691 0.8218	0.06 3.57	8.70 57.16	636.56 800.91
WT 50mM 68 pN	1.5233	0.0956	0.0050	0.0874	0.1887	0.7239	0.66	10.46	199.68
	0.4821 7.3087	0.0143 0.2429	0.0040 0.0056	0.0649 0.2198	0.1221 0.3548	0.3953 0.7643	0.14 2.07	4.12 70.08	178.31 250.41
WT 50mM 74 pN	23.7187	0.1055	0.0087	0.3150	0.5152	0.1697	0.04	9.48	114.44
	0.2335 44.2823	0.0495 0.1323	0.0051 0.0129	0.1597 0.7889	0.1345 0.6289	0.0323 0.2382	0.02 4.28	7.56 20.19	77.53 194.85
WT 50mM 93 pN	1.8677	0.2205	0.0185	0.3008	0.6167	0.0825	0.54	4.53	54.00
	0.8525 3.6589	0.1434 0.2883	0.0107 0.0300	0.2281 0.5206	0.4123 0.6732	0.0396 0.1219	0.27 1.17	3.47 6.98	33.30 93.39
WTGCf 50mM 29 pN	0.3818	0.0250		0.9539	0.0461		2.62	40.00	
	0.3598 0.4072	0.0198 0.0332		0.9368 0.9689	0.0310 0.0631		2.46 2.78	30.15 50.53	
WTGCf 50mM 35 pN	1.0263	0.2331		0.9370	0.0630		0.97	4.29	
	0.9606 1.4694	0.1381 0.5954		0.5704 0.9713	0.0286 0.4233		0.68 1.04	1.68 7.24	
WTGCf 50mM 40 pN	3.6937	1.4405		0.4913	0.5087		0.27	0.69	
	3.2017 4.4938	1.2980 1.5661		0.3824 0.6074	0.3924 0.6168		0.22 0.31	0.64 0.77	
WTperm 50mM 19pN	7.1863	1.9324		0.9528	0.0472		0.14	0.52	
	6.8488 100.0000	1.5950 5.4160		0.9176 0.9959	0.0039 0.0823		0.01 0.15	0.18 0.63	

Table 2. Overview of extracted kinetic rates and probabilities. The probabilities are calculated from the extracted rates using eqns. 4–7. Lower and upper 1-σ CIs are shown left and right below each value respectively.

Dataset	k10 (1/s)	k12 (1/s)	k20 (1/s)	k23 (1/s)	k30 (1/s)	P(1)	P(2)	P(3)
E49K 50mM 59 pN	0.7175	0.6799	0.2088	0.0344	0.0011	0.5134	0.4178	0.0687
	0.6178 0.8735	0.4164 1.0609	0.1683 0.2431	0.0260 0.0431	0.0009 0.0013	0.4313 0.6088	0.3189 0.5016	0.0518 0.0825
E49KGCf 50mM 19 pN	0.4013	0.9642	0.1689	0.0548	0.0646	0.2939	0.5331	0.1730
	0.3370 0.4534	0.4289 1.5777	0.1259 0.2018	0.0145 0.1071	0.0430 0.0774	0.2210 0.4419	0.4632 0.5924	0.0594 0.2666
E49KGCf 50mM 24 pN	1.6523	0.1321	0.3476	0.0929	0.0519	0.9260	0.0584	0.0156
	1.5699 1.7387	0.0962 0.2959	0.2455 0.9245	0.0446 0.1390	0.0368 0.0919	0.8486 0.9445	0.0425 0.1294	0.0087 0.0311
F140A 50mM 47 pN	2.9297	4.4037	0.0357	0.0374	0.0086	0.3995	0.2933	0.3072
	2.0672 5.9511	3.5706 6.4214	0.0262 0.0896	0.0125 0.2314	0.0060 0.0116	0.3375 0.5115	0.1539 0.4174	0.1632 0.3969
F140A 50mM 50 pN	0.4068	1.2360	0.0427	0.0109	0.0097	0.2476	0.5992	0.1532
	0.3102 70.4627	0.5425 2.0994	0.0369 0.0697	0.0063 0.0462	0.0072 0.0183	0.2049 0.9809	0.0083 0.6533	0.0085 0.2249
F140A 50mM 54 pN	7.5623	12.1052	0.1464	0.0167	0.0298	0.3845	0.5526	0.0629
	2.3778 19.4368	6.9996 12.8166	0.1351 0.1633	0.0104 0.0330	0.0214 0.0463	0.2472 0.6264	0.3180 0.6683	0.0329 0.1050
F140A 50mM 59 pN	1.7161	3.0050	0.3408	0.0099	0.0181	0.3635	0.6185	0.0180
	1.3277 2.3275	2.0426 4.3437	0.3072 0.3759	0.0057 0.0156	0.0153 0.0216	0.3258 0.4231	0.5566 0.6532	0.0102 0.0271
F140AGCf 50mM 35 pN	0.3205	0.2064	0.0799			0.6082	0.3918	
	0.2516 0.4502	0.0661 0.5809	0.0509 0.1070			0.4230 0.7902	0.2094 0.5746	
F140AGCf 50mM 40 pN	0.6519	0.4195	0.1757			0.6085	0.3915	
	0.5387 1.1811	0.1928 1.7212	0.1340 0.2331			0.3942 0.7371	0.2628 0.6057	
F140AGCf 50mM 47 pN	2.1976	3.9695	0.8115			0.3563	0.6437	
	1.8948 2.5662	3.1183 4.8638	0.7731 0.8504			0.3258 0.3966	0.6031 0.6741	
H144A 50mM 24 pN	1.6761	13.3167	0.0408	0.0171	0.0042	0.1118	0.6262	0.2620
	0.0597 99.8145	0.1211 11.2308	0.0284 0.0472	0.0101 0.0244	0.0034 0.0054	0.0948 0.9981	0.0014 0.6512	0.0005 0.2954
H144A 50mM 35 pN	99.5198	0.4802	0.0645	0.0133	0.0071	0.9952	0.0040	0.0008
	0.0692 98.7552	0.0206 3.7824	0.0123 0.0654	0.0012 0.0164	0.0020 0.0092	0.1038 0.9927	0.0060 0.7292	0.0014 0.1699
H144A 50mM 40 pN	0.2970	0.6362	0.1357	0.0156	0.0101	0.3183	0.6115	0.0702
	0.2693 2.1655	0.3850 10.4933	0.1214 0.1672	0.0120 0.0193	0.0087 0.0126	0.1498 0.4269	0.5092 0.7732	0.0527 0.0848
H144A 50mM 47 pN	0.5317	98.4881	0.5196	0.0184	0.0211	0.0054	0.9606	0.0340
	0.5321 0.6938	0.0348 99.1527	0.1296 0.5133	0.0133 0.0338	0.0164 0.0255	0.0066 0.9521	0.0454 0.9545	0.0144 0.0392
H144A 50mM 59 pN	4.7245	1.2947	2.2411	0.0780	0.4642	0.7849	0.2079	0.0072
	4.2569 5.4003	0.7782 93.3624	1.7924 3.7682	0.0272 0.5556	0.3036 1.6819	0.0566 0.8541	0.1179 0.6938	0.0026 0.0699
H144AGCf 50mM 19 pN	3.2712	7.6006	1.2214			0.3009	0.6991	
	2.2090 16.4183	3.0051 11.3265	1.1389 1.2910			0.2984 0.6109	0.3880 0.7015	
Q250A 200mM 59pN	41.2326	9.6673	0.0757	0.0168	0.0046	0.8101	0.1555	0.0345
	0.1296 62.9968	0.2685 15.1011	0.0607 0.0850	0.0105 0.0227	0.0038 0.0057	0.4522 0.9365	0.0302 0.4397	0.0015 0.1114
Q250A 50mM 59 pN	0.7363	6.9334	0.0272	0.0385	0.0043	0.0960	0.3742	0.5298
	0.0685 1.3946	0.2295 9.2923	0.0120 0.0419	0.0158 0.0960	0.0035 0.0051	0.0754 0.2423	0.2475 0.4587	0.3921 0.6220
Q250A 50mM 93 pN	99.8000	0.2000	0.5982	0.1269	0.0530	0.9980	0.0016	0.0003
	0.6705 99.8517	0.1319 1.8363	0.1116 0.6188	0.0141 0.1521	0.0196 0.0675	0.4295 0.9985	0.0012 0.4628	0.0002 0.0938
WT 200mM 74 pN	3.1162	10.6808	0.0238	0.0248	0.0048	0.2259	0.3789	0.3952
	0.1255 9.2143	0.6257 14.0952	0.0134 0.0460	0.0091 0.1560	0.0036 0.0066	0.1321 0.4473	0.1766 0.5026	0.2161 0.5324
WT 200mM 93 pN	0.5422	0.5497	0.1486	0.0139	0.0311	0.4965	0.4605	0.0429
	0.4687 0.6504	0.4218 1.0533	0.1302 0.1914	0.0081 0.2583	0.0224 0.0957	0.3657 0.5605	0.3760 0.5497	0.0252 0.2822
WT 350mM 74 pN	2.3591	10.2785	0.0289	0.0180	0.0071	0.1867	0.5009	0.3125
	0.9963 4.6580	7.3901 13.0933	0.0243 0.0342	0.0128 0.0259	0.0063 0.0082	0.1142 0.3076	0.3946 0.5647	0.2307 0.3847
WT-mmTer 50mM 59 pN	0.0354	0.3196	0.0058	0.0189	0.0018	0.0844	0.1659	0.7497
	0.0220 0.0819	0.1340 3.1424	0.0031 0.0149	0.0061 0.0759	0.0017 0.0021	0.0113 0.1427	0.1212 0.2675	0.6378 0.8222
WT 50mM 59 pN	0.0724	0.7120	0.0066	0.0277	0.0014	0.0923	0.1756	0.7321
	0.0348 0.1660	0.2442 14.2307	0.0034 0.0147	0.0127 0.0925	0.0012 0.0016	0.0514 0.1529	0.1250 0.2689	0.6171 0.7943
WT 50mM 68 pN	0.1548	1.3685	0.0228	0.0728	0.0050	0.1016	0.2147	0.6837
	0.0787 0.3782	0.3884 6.7703	0.0082 0.0454	0.0059 0.1986	0.0040 0.0056	0.0787 0.2401	0.1402 0.4683	0.2857 0.7249
WT 50mM 74 pN	7.5284	16.1903	0.0815	0.0241	0.0087	0.3174	0.5270	0.1556
	0.1225 31.3348	0.1107 15.5270	0.0320 0.0958	0.0083 0.0388	0.0051 0.0129	0.1700 0.7980	0.1516 0.6338	0.0264 0.2113
WT 50mM 93 pN	0.6994	1.1683	0.1942	0.0264	0.0185	0.3745	0.5508	0.0748
	0.4852 1.0736	0.3525 2.5548	0.1275 0.2459	0.0117 0.0462	0.0107 0.0300	0.2877 0.5864	0.3557 0.6237	0.0356 0.1077
WTGCf 50mM 29 pN	0.3654	0.0164	0.0250			0.9569	0.0431	
	0.3439 0.3888	0.0109 0.0228	0.0198 0.0332			0.9421 0.9711	0.0289 0.0579	
WTGCf 50mM 35 pN	0.9763	0.0500	0.2331			0.9513	0.0487	
	0.9197 1.1469	0.0244 0.3774	0.1381 0.5954			0.7458 0.9754	0.0246 0.2529	
WTGCf 50mM 40 pN	2.5475	1.1462	1.4405			0.6897	0.3103	
	2.3883 2.7553	0.7434 1.7795	1.2980 1.5661			0.6008 0.7686	0.2313 0.3976	
WTperm 50mM 19pN	6.9384	0.2479	1.9324			0.9655	0.0345	
	6.5977 99.5651	0.1189 0.4407	1.5950 5.4160			0.9421 0.9968	0.0032 0.0578	

The exponential fit has the general form of:

$$P(t) = \sum_{i=1}^{N} A_i e^{-k_i t} \qquad (1)$$

where *N* is the number of exponentials determined by the BIC. In our kinetic model (**Supplementary Fig. 4a**) the general rates (k_i) and probabilities (A_i) are expressed in terms of the five state associated rates, with

$$\begin{aligned}
k_1 &= k_{10} + k_{12} \\
k_2 &= k_{20} + k_{23} \\
k_3 &= k_{30} \\
A_1 &= \frac{k_{10}^2 + k_{10}k_{12} - k_{10}k_{20} - k_{12}k_{20} - k_{10}k_{23} - k_{10}k_{30} + k_{20}k_{30} + k_{23}k_{30}}{(k_{10} + k_{12} - k_{20} - k_{23})(k_{10} + k_{12} - k_{30})} \\
A_2 &= \frac{k_{12}k_{20} - k_{12}k_{30}}{(k_{10} + k_{12} - k_{20} - k_{23})(k_{20} + k_{23} - k_{30})} \\
A_3 &= \frac{k_{12}k_{23}}{(k_{10} + k_{12} - k_{30})(-k_{20} - k_{23} + k_{30})} \qquad (2)
\end{aligned}$$

for the 3-exponential model, and

$$\begin{aligned}
k_1 &= k_{10} + k_{12} \\
k_2 &= k_{20} \\
A_1 &= \frac{k_{10} - k_{20}}{k_{10} + k_{12} - k_{20}} \\
A_2 &= \frac{k_{12}}{k_{10} + k_{12} - k_{20}} \qquad (3)
\end{aligned}$$

for the 2-exponential model.

$$P(1) = \frac{k_{10}}{k_{10} + k_{12}} \qquad (4)$$

$$P(2) = \frac{k_{12}}{k_{10} + k_{12}} \qquad \text{(2-exp fit)} \qquad (5)$$

$$P(2) = \frac{k_{12}}{k_{10} + k_{12}} \cdot \frac{k_{20}}{k_{20} + k_{23}} \qquad \text{(3-exp fit)} \qquad (6)$$

$$P(3) = \frac{k_{12}}{k_{10} + k_{12}} \cdot \frac{k_{23}}{k_{20} + k_{23}} \qquad (7)$$